Journal of Materials Chemistry C

High Piezoelectricity of BaTiO3-CaTiO3-BaSnO3 Lead-Free Ceramics

Journal:	*Journal of Materials Chemistry C*
Manuscript ID:	TC-ART-01-2014-000155.R1
Article Type:	Paper
Date Submitted by the Author:	21-Mar-2014

Complete List of Authors:	Zhu, Li-Feng; University of Science and Technology Beijing, Zhang, Bo-Ping; University of Science and Technology Beijing, Zhao, Lei; University of Science and Technology Beijing, Li, Jing-Feng; Tsinghua University, State Key Laboratory of New Ceramics and Fine Processing, Department of Materials Science and Engineering

High Piezoelectricity of $BaTiO_3$-$CaTiO_3$-$BaSnO_3$ Lead-Free Ceramics

Li-Feng Zhu [a], Bo-Ping Zhang [a,*], Lei Zhao [a], Jing-Feng Li [b]

A series of solid solutions $BaTiO_3$-x($0.4CaTiO_3$-$0.6BaSnO_3$) (abbreviated as BT-x(CT-BS), x=0.00-0.20 mol) were prepared to search for a high performance lead-free piezoelectric ceramics. Through contents tailoring, a complex phase transition was confirmed by X-ray diffraction and Raman spectra as well as temperature dependence of dielectric constant, which is from tetragonal(T)-orthorhombic(O) coexistence at $0 \leq x \leq 0.12$ to rhombohedral(R)-O-T and R-O/T-cubic(C) multiphase coexistence at x=0.16 and 0.20, respectively. The lower E_C=1.31 kV/cm and higher P_r=9.48 μm/cm^2 as well as high piezoelectric response d_{33}=570 pC/N were achieved in BT-x(CT-BS) ceramics at an optimal composition of x=0.16. The ultrahigh converse piezoelectric coefficient d_{33}^*=1444 pm/V and strain 0.070% which are the highest value reported so far in lead-free ceramics also were achieved at x=0.16, suggesting that BT-x(CT-BS) system is a promising lead-free alternative material for electromechanical actuator applications.

[a] School of Materials Science and Engineering, University of Science and Technology Beijing, Beijing 100083, China. *E-mail: bpzhang@ustb.edu.cn; Tel: +86-10-62334195*
[b] State Key Laboratory of New Ceramics and Fine Processing, School of Materials Science and Engineering, Tsinghua University, Beijing 100084, China

Introduction

Lead-based piezoelectric materials such as $Pb(Zr,TiO_3)$ (PZT) have been widely used in various types of sensors, actuators, buzzers, medical ultrasonic transducers and other electronic devices because of their excellent piezoelectric properties and good temperature stability [1, 2]. However, these lead-based ceramics are facing global restrictions due to Pb toxicity. Therefore, it is urgent to develop lead-free alternative materials with comparable piezoelectric and electromechanical properties to their lead-based counterparts. Recently, a series of typical lead-free systems such as $BaTiO_3$ (BT), $(Bi_{0.5}Na_{0.5})TiO_3$ and $(K_{0.5}Na_{0.5})NbO_3$ based ceramics, have been highlighted to substitute for PZT [2-5]. Among them, BT based ceramics with excellent electrical properties are considered as one of promising candidates for lead-based piezoelectric ceramics [6-8]. High piezoelectric constants d_{33}=530 pC/N, 550 pC/N and 620 pC/N were achieved in $Ba(Sn_{0.12}Ti_{0.88})O_3$-$30(Ba_{0.7}Ca_{0.3})O_3$ [6], $Ba(Ti_{0.8}Hf_{0.2})O_3$-$50(Ba_{0.7}Ca_{0.3})TiO_3$ [7] and $Ba(Zr_{0.2}Ti_{0.8})O_3$-$50(Ba_{0.7}Ca_{0.3})TiO_3$ (BZT-50BCT) [8] systems, respectively.

It is well known that the morphotropic phase boundary (MPB) separating rhombohedral (*R*) and tetragonal (*T*) phases plays an important role in enhancing piezoelectric properties for PZT piezoelectric family. Similar to MPB behavior in PZT system, the high piezoelectric property of BZT-50BCT ceramic is also attributed to MPB behavior where *R* and *T* two-phase coexisted [8]. Ultrahigh relative dielectric constant 75000 and piezoelectric coefficient d_{33}=697 pC/N have achieved in $BaTiO_3$-$x$$BaSnO_3$ ceramics at 40 °C in the vicinity of two converged triple points with multiphase coexistence [9]. The giant dielectric and piezoelectric properties near the phase boundary or a point of multiphase coexistence might originate from the low energy barriers, which can greatly facilitate the polarization rotation and extension [8-10].

Therefore, it is a good choice to design two-phase or multiphase coexistence near room temperature to enhance the piezoelectric property. It is known that BT ceramic shows a *T*-symmetry at room temperature and becomes orthorhombic (*O*)-symmetry and *R*-symmetry below 0 °C and -90 °C, respectively. The phase transformation temperature for *R* to *O* ($T_{R\text{-}O}$) and *O* to *T* ($T_{O\text{-}T}$) can be shifted to room temperature by

replacing Ti^{4+} with Sn^{4+} at B-sites in $BaTiO_3$-$x$$BaSnO_3$ system [9]. A-site replacement of Ba^{2+} by Ca^{2+} was found to reduce $T_{R\text{-}O}$ and $T_{O\text{-}T}$ to a low temperature, along with a little effect on Curie temperature (T_C) in $BaTiO_3$-$x$$CaTiO_3$ system [11]. It is expected that a compositional boundary of two-phase or multiphase coexistence is obtainable near room temperature in $BaTiO_3$-$CaTiO_3$-$BaSnO_3$ ternary system. Figure 1 summaries a series of recently reported phase structure of $BaTiO_3$-$CaTiO_3$-$BaSnO_3$ ternary system near BT-rich corner in a phase diagram. A similar phase transformation from *O* to *T* at room temperature was detected in $(Ba_{1-x}Ca_x)(Ti_{0.96}Sn_{0.04})O_3$ ($0.01\leq x\leq 0.04$) [12], $(Ba_{1-x}Ca_x)(Ti_{0.94}Sn_{0.06})O_3$ ($0.01\leq x\leq 0.04$) [13] and $(Ba_{1-x}Ca_x)(Ti_{0.92}Sn_{0.08})O_3$ ($0.00\leq x\leq 0.06$) [14] ceramics. The component of *O* and *T* two-phase coexistence is at x=0.02, 0.03 and 0.05 for above three systems as shown in Fig. 1 by symbol "◊", which follows certain component of (1-x)$BaTiO_3$-x(0.4$CaTiO_3$-0.6$BaSnO_3$) as shown by a dotted line. Compositional zones Ⅰ and Ⅱ indicate *O* and *T* two-phase separated by this (1-x)$BaTiO_3$-x(0.4$CaTiO_3$-0.6$BaSnO_3$) components. On the other hand, $Ba(Sn_xTi_{1-x})O_3$ [9] and $Ba(Sn_{0.12}Ti_{0.88})O_3$-$x$$(Ba_{0.7}Ca_{0.3})O_3$ [6] ceramics show a phase transition of *R*-*O* and *R*/*PC*-*T* at x=0.09 and 0.3, respectively, which suggests that *R*-phase is situated in zone Ⅲ. Consequently, it is possible to obtain *R*/*PC*-*O*-*T* multiphase coexistence compositions at room temperature in BT-x(CT-BS) system, which possess high piezoelectric property. In the present study, the phase structure and electrical properties for a series of BT-x(CT-BS) ceramics were investigated. An ultrahigh converse piezoelectric coefficient d_{33}^*=1444 pm/V and unipolar strain (0.070%) were achieved at the multiphase coexistence compositions. This results suggest that BT-x(CT-BS) system is a promising lead-free alternative material for electromechanical actuator applications.

Experimental

Barium carbonate ($BaCO_3$, 99.0%), calcium carbonate ($CaCO_3$, 99%), stannic oxide (SnO_2, 99.5%) and titanium dioxide (TiO_2, 99.0%) were used as raw materials. These powders were weighed according to the compositions of $BaTiO_3$-x(0.4$CaTiO_3$-0.6$BaSnO_3$) (abbreviated as BT-x(CT-BS), x=0.00-0.20 mol) and

mixed with alcohol. After drying the slurry and calcining at 1300 ℃ for 4 h, the resultant powders were remixed and pressed into disks of 10 mm in diameter and 1.5 mm in thickness under 80 MPa using 2 wt% polyvinyl alcohol (PVA) as the binder, followed by burning the binder at 650 ℃ by 5 ^{o}C/min and for 1 h. The samples were cooled to room temperature and then rose directly to 1480 ℃ by 5 ℃/min and held for 2 h. The sintered specimen was coated with silver paint on the upper and bottom surfaces and fired at 600 ℃ for 30 min for electrical measurements. The poling was performed under a dc field of 4 kV/mm at room temperature for 30 min in a silicone oil bath.

The crystal structure was studied by using XRD with a Cu $K\alpha$ radiation (λ=1.5406 Å) filtered through a Ni foil (Rigaku; RAD-B system, Tokyo, Japan). The microstructure of the sintered samples was observed by field emission scanning electron microscopy (FESEM, SUPRATM 55, Japan). The temperature dependence of dielectric properties was examined using a programmable furnace with an LCR analyzer (TH2828S) at 1 kHz in temperature range of -40 ℃ to 160 ℃. The Raman spectra were measured by HR800 Microscopic Confocal Raman spectrometer (Horiba Jobin Yvon Company, French), in which the light source of He-Ne gas laser, laser wavelength of 633 nm, using semiconductor cooling type of CCD detector. First, the sample was cooled to -150 ℃ and heated to 150 ℃. During the heating, the sample was held at each temperature for more than 5 min before the Raman spectrum was measured. Ferroelectric hysteresis loops were measured using a ferroelectric tester (RT6000HVA, Radiant Technologies, Inc., Albuquerque, NM). The electric-field-induced strains were measured by using an attachment onto TF ANALYZER 1000 ferroelectric measuring system (aixACCT Systems GmbH, Germany). The piezoelectric properties were measured using a quasi-static piezoelectric coefficient d_{33} testing meter (ZJ-3A, Institute of Acoustics, Chinese Academy of Sciences, Beijing, China). The planar electromechanical coupling coefficient k_p and the mechanical quality factor Q_m were determined by resonance-antiresonance method using an Agilent 4294A precision impedance analyzer (Hewlett-Packard, Palo Alto, CA).

Results and discussion

1. XRD analysis

Figure 2 shows room temperature X-ray diffraction patterns of BT-x(CT-BS) (x=0.00, 0.04, 0.08, 0.12, 0.16, 0.20) ceramics. All ceramics exhibit a pure perovskite structure without any trace of impurity, suggesting that both Ca^{2+} and Sn^{4+} have diffused into the host lattice to form a solid solution. The standard diffraction peaks cited from $BaTiO_3$ with *R*, *O* and *T*-symmetries (PDF#85-0368, PDF#81-2200 and PDF#05-0626) are indicated by vertical lines for comparison. The diffraction peaks of the composition of x=0.00 correspond well with *T*-symmetry PDF#05-0626. Unlike the stronger $(200)_T$ peak in the PDF#05-0626, the peak intensity of $(002)_T$ is higher than that of $(200)_T$ in the composition of x=0.00 as shown in the enlarged XRD patterns of angles ranged from 44^o to 46^o in Fig. 2b, which indicates that the sample also consists of *O*-phase (PDF#81-2200). There are three peaks around 56^o which are similar to the standard card PDF#81-2200, further confirming the existence of *O*-phase in the pure $BaTiO_3$. As increasing x, the diffraction peak of $(200)_T$ around 45^o gradually shifts to a lower angle as shown in Fig. 2b, along with a constant $(002)_T$ peak. As $x\geq0.12$, the diffraction peak of $(200)_T$ merges into a broad peak with $(002)_T$ peak, suggesting that the main phase undergoes an obvious phase transition. The three peaks around 56^o at x=0.00 also gradually merge into two peaks at $0.04\leq x\leq0.08$ and one broad peak at $x\geq0.12$, which indicates that the phase structure of samples changed as increasing x. However, it is difficult to define the phase structure for the samples at $0.12\leq x\leq0.20$, because of the broad diffraction peaks near 45^o and 56^o as shown in Fig. 2b. More evidence should be adduced to identify the phase structure of samples at $0.12\leq x\leq0.20$.

2. Temperature dependence of dielectric constant and phase diagram

Figure 3 shows the temperature dependence of dielectric constant ε_r and dielectric loss factor $tan\delta$ for BT-x(CT-BS) ($0.00\leq x\leq0.20$) ceramics, which were measured at 1 kHz between -50 ^{o}C and 140 ^{o}C. Two phase-transition points were detected as x=0.00, which correspond to ferroelectric-ferroelectric phase transition T_1 and ferroelectric-paraelectric phase transition T_C, respectively. Adding x produces the

appearance of three transition peaks corresponding to T_2, T_1 and T_C in the temperature range between -50 °C to 140 °C at $0.04 \leq x \leq 0.16$. T_C is about 134 °C at x=0.00 and emerges a linear declining trend with increasing x until 39 °C at x=0.20, which is caused by replacing Ti^{4+} with Sn^{4+}at B-sites [15]. Along with the decreased T_C, both T_2 and T_1 arise with increasing x and three transition peaks merge into one peak T_C at x=0.20. Similar variation tendency of phase transition points T_2, T_1 and T_C is also noticed in *tanδ*-temperature curve.

Figure 4 shows the phase diagram of BT-x(CT-BS) ceramics based on the ε_r-temperature curve. Along with the linearly decreased T_C for all samples, both T_2 and T_1 lines arise with increasing x from 0.00 to 0.20 and gradually merge with T_C line. T_1 corresponding to phase transition temperature between $phase_{II}$ and $phase_{III}$ slowly increases from 18 °C to 39 °C as increasing x from 0.00 to 0.20. Because of T_1 near room temperature, the $phase_{II}$ and $phase_{III}$ should exist at room temperature in the samples at $0.00 \leq x \leq 0.20$. Comparing with the flat T_1, T_2 defined as the phase transition temperature between $phase_{III}$ and $phase_{IV}$ rapidly rises from -37 °C to 39 °C as increasing x from 0.04 to 0.20. Since increased T_2 crosses room temperature as $0.16 \leq x \leq 0.20$, the $phase_{IV}$ should appear near room temperature in the samples. We speculate that $phase_{II}$, $phase_{III}$ and $phase_{IV}$ may coexist as $0.16 \leq x \leq 0.20$ while the former two phases coexist as $0.00 \leq x \leq 0.12$ at room temperature.

3. Raman spectra

Figure 5a shows the temperature dependence of the Raman spectra for the pure BT ceramic, which indicates an obvious evolution of phase transformation. The spectrum measured at -150 °C shows the presence of the following Raman-active modes: v_3(LO), v_3(TO), v_4(LO), v_2(LO, TO), v_1(TO), v_1(LO) situated at around 168 cm^{-1}, 185 cm^{-1}, 225 cm^{-1}, 308 cm^{-1}, 525 cm^{-1}, 715 cm^{-1}, respectively, which corresponds to *R*-phase characteristic, especially v_3(LO) peak at 169.8 cm^{-1} and two dips between v_3(LO) and v_3(TO) at 178 cm^{-1} as well as v_3(TO) and v_4(LO) peaks at 194 cm^{-1}. All Raman-active modes are in agreement with those in the literatures [16-20]. As increasing the test temperature (T_t) over -50 °C, the

R-phase characteristic v_3(LO) peak at 169.8 cm^{-1} disappears, while v_3(TO) and the other peaks widen, along with the disappearance of the dip between v_3(TO) and v_4(LO) peaks at 194 cm^{-1} [20]. This results indicate that the phase structure of BT which is *R*-phase at $T_t \leq -50\ ^oC$ completely transforms into *O*-phase at $T_t > -50\ ^oC$ [20]. As further increasing T_t to 20 °C, v_3(TO) peak at 180 cm^{-1} disappears, indicating that the phase structure changed from *O*-phase to *T*-phase [20]. At $T_t \geq 150$ °C, v_1(LO) peak near 715 cm^{-1} and the dip between v_3(LO) at 168 cm^{-1} and v_3(TO) at 185 cm^{-1} disappear, suggesting that the phase structure of sample changes into cubic (*C*)-phase from *T*-phase [20]. The temperatures of phase transitions for *R*-*O*, *O*-*T*, and *T*-*C* are near -50 °C, 20 °C and 150 °C, respectively, which is consistent with dielectric constant ε_r and phase diagram as shown in Figs. 3 and 4, respectively. Thus, the $phase_{I}$, $phase_{II}$, $phase_{III}$ and $phase_{IV}$ shown in Fig. 4 correspond to *C*, *T*, *O* and *R* phase, respectively. Concerning the evolution of phase structure, the change in the modes of v_3(LO), v_3(TO) and v_2(LO, TO) peaks with temperature for sample at x=0.00 is detailedly shown in Fig. 5b.

Figure 6 shows the temperature dependence of the Raman spectra of BT-x(CT-BS) ceramics for x=0.12 (a1, a2), 0.16 (b1, b2) and 0.20 (c1, c2), respectively. Comparing with pristine BT shown in Fig. 5a, the peaks of the samples at $0.12 \leq x \leq 0.20$ widen and only one dip between v_3(LO) and v_4(LO) peaks is detected. Main modes v_3(LO), v_3(TO), v_4(LO), v_2(LO, TO), v_1(TO), v_1(LO) situated at around 168 cm^{-1}, 185 cm^{-1}, 225 cm^{-1}, 308 cm^{-1}, 525 cm^{-1}, 715 cm^{-1}, respectively, are still observable at -150 °C as x=0.12, 0.16 and 0.20 as shown in Figs. 6a1, 6b1 and 6c1, suggesting that the phase structure is *R*-phase. As increasing T_t, *R*-phase characteristic peak at 169.8 cm^{-1} as marked by dotted lines disappears over 0 °C, 20 °C and 40°C as x=0.12, 0.16 and 0.20, respectively, indicating the absence of *R* phase. The variation temperature of *R*-phase in the Raman spectra is consistent with that in ε_r-temperature curve.

No obvious change on the modes as x=0.12 is observed at $20 \leq T_t < 60$ °C as shown in the enlarged Raman spectra between 100 and 320 cm^{-1} in Fig. 6a2. This is inconsistent with phase diagram shown in Fig. 4, where *O*-*T* phase transition exists at 35 °C. The absence of *O*-*T* phase transition shown in the Raman

spectra at $20 \leq T_t < 60$ °C is due to the coexistence of *O* and *T* two-phases or their similar Raman spectra characteristics between *O* and *T* phases. At $T_t \geq 80$ °C, the dip between v_3(LO) at 168 cm^{-1} and v_3(TO) at 185 cm^{-1} disappears along with absent v_1(LO) at 715 cm^{-1}, indicating the appearance of *C*-phase. *T*-*C* phase transition happened at 80 °C, which is consistent with phase diagram in Fig. 4.

Different from x=0.12, *R*-phase characteristic v_3(LO) at 169.8 cm^{-1} disappears at higher $T_t \geq 40$°C as shown in Fig. 6b2 as x=0.16, suggesting that *R*-phase exists at $-150 \leq T_t < 40$°C. Since *R*-phase still exists at $20 \leq T_t < 40$°C and the phase transition between *O*- and *T*-phase happens at 38 °C shown in Fig. 3 for the sample as x=0.16, *R*-*O*-*T* multiphase should be coexisted at room temperature. This result is consistent with phase diagram in Fig. 4. As further increasing T_t to 60 °C, the disappearance of the dip between v_3(LO) at 168 cm^{-1} and v_3(TO) at 185 cm^{-1} indicates that the phase structure of sample turns into *C*-phase.

Among three samples, *R*-phase characteristic v_3(LO) at 169.8 cm^{-1} as marked by dotted line exists at $T_t > 40$°C as x=0.20 as shown in Fig. 6c2, suggests the increased transition temperature of *R*-phase that is will consistent with the variation of T_2 with increasing x in phase diagram in Fig. 4. The disappearance of the dip between v_3(LO) at 168 cm^{-1} and v_3(TO) at 185 cm^{-1} happens at $T_t \geq 40$°C, suggesting that the forming temperature of *C*-phase is about 40 °C and lowered with increasing x. Thus, both *R*-phase and *C*-one should appear at room temperature as x=0.20. This phenomenon is consistent with the phase diagram in Fig. 4, which shows that the increasing T_2 and decreased T_C merged a point as increasing x to 0.20. However, it is difficult to exclude *T*- and *O*-phase existence at room temperature because of most features of the Raman modes from *R* phase include in *O* and/or *T* phase [20]. Thus, the phase structure of sample should consist of *R*-*O*/*T*-*C* or *R*-*O*-*T*-*C* multiphase coexistence. Since the quadruple point (*R*-*O*-*T*-*C*) would break Gibbs Phase Rule, the phase structure of sample at x=0.20 is *R*-*O*/*T*-*C* multiphase coexistence near room temperature rather than *R*-*O*-*T* ones.

4. **Microstructure**

Figure 7 shows SEM images of thermally etched surface for BT-x(CT-BS) ($0.00 \leq x \leq 0.20$) ceramics

sintered at 1480 °C. The composition of x=0.00 shown in Fig. 2a has a large average grain size of about 70 μm, which decreases monotonously to 6.5 μm as increasing x to 0.20 as shown in Fig. 7f. Since the densification sintering temperature is above 1700 °C for BS ceramic that is higher than 1300 °C for BT ceramic [21], the replacement of Ti^{4+} by Sn^{4+} in BT-x(CT-BS) ceramics should increase the densification sintering temperature, resulting in the refined grain size with increasing the BS content at a fixed sintering temperature such as 1480 °C. Shen [22] reported that small grain sizes are in favour of high performance in BT ceramics. We speculate that samples at x=0.16 and 0.20 would have higher piezoelectric property than others.

5. Ferroelectricity and piezoelectricity

Figure 8 shows the *P*-*E* hysteresis loops of BT-x(CT-BS) ceramics with x=0.00, 0.08 and 0.16 measured at room temperature, being a typical ferroelectric polarization hysteresis loops for all samples. The inset in Fig. 8 illustrates the variation in the remnant polarization P_r and coercive field E_C. P_r firstly increases from 6.23 μm/cm^2 at x=0 to 9.48 μm/cm^2 at x=0.16, and then rapidly decreases to 3.25 μm/cm^2 at x=0.20, whereas E_C decreases from 2.62 kV/cm at x=0.00 to 0.81 kV/cm at x=0.20. The decrease of E_C reveals that the samples became more "soft" as increasing x with respect to the electric field. The sample of "soft" indicates that free energy profile for polarization rotation is anisotropically flattened at the two-phase and multiphase coexistence [9]. However, the lower E_C reveals that there need lower energy barriers for polarization rotation, which is due to multiphase coexistence of *R*-*O*-*T* at x=0.16 and *R*-*O*/*T*-*C* at x=0.20. This low energy barrier can greatly facilitate the polarization rotation and effectively enhance the piezoelectric property. The ceramic of *R*, *O* and *T* three-phase coexistence at x=0.16 exhibits a lower E_C=1.31 kV/cm than 1.68 kV/cm in $Ba(Zr_{0.2}Ti_{0.8})TO_3$-$50(Ba_{0.7}Ca_{0.3})TiO_3$ [8] and 3.0 kV/cm in $Ba(Ti_{0.88}Sn_{0.12})O_3$-$30(Ba_{0.7}Ca_{0.3})TiO_3$ systems [6] shown in Table 1, which indicates that BT-x(CT-BS) ceramics are more "soft" than them. Thus, we speculate that BT-x(CT-BS) ceramics may possess a superior piezoelectricity to $Ba(Zr_{0.2}Ti_{0.8})TO_3$-$50(Ba_{0.7}Ca_{0.3})TiO_3$ and $Ba(Ti_{0.88}Sn_{0.12})O_3$-$30(Ba_{0.7}Ca_{0.3})TiO_3$ systems.

Figure 9 shows the bipolar Strain-electric field (*S*-*E*) loops of BT-*x*(CT-BS) ceramics as a function of *x* measured at 2000 V/mm at room temperature. All samples exhibit a butterfly-shaped *S*-*E* loops that is typical for ferroelectric materials. A pronounced enhancement in the maximum positive strain (S_{pos}) response from 0.093% at *x*=0.00 to 0.134% at *x*=0.16 is observed. However, the electric-field-induced butterfly-like hysteretic strain loops in ferroelectrics are basically due to both the intrinsic and extrinsic contributions. The intrinsic contribution is mainly referred to the variation of lattice distortion. A common approach to enhance the intrinsic contribution (lattice strain) used to be the adjustment of the chemical compositions within a coexistence zone of two or more ferroelectric phases, which effectively facilitate the polarization rotation and extension [23-25]. The extrinsic contribution to strains is mainly from the domain switching, during which ferroelectric materials change their spontaneously polarized states along the applied electric field direction. The magnitude of the strain generated during domain switching depends on the type of the domains being switched and the extent of the lattice anisotropy [26]. Thus, the high S_{pos}=0.134% for BT-*x*(CT-BS) ceramics at *x*=0.16 is related to the intrinsic which is due to *R*, *O* and *T* three-phase coexistence proved by Raman spectra, and extrinsic contributions which is due to the low E_C, corresponding to the easiness of domain rotation, respectively.

Figure 10 shows the unipolar electric-field-induced strain curves measured at 500 V/mm for BT-*x*(CT-BS) ceramics with *x*=0.00, 0.04, 0.08, 0.12, 0.16 and 0.20 at room temperature. The converse piezoelectric coefficient ($d_{33}^*=S_{max}/E_{max}$) of BT-*x*(CT-BS) ceramics for all studied compositions is summarized in the inset of Fig. 10. Similar to bipolar strain, the unipolar strain also increases with increasing *x* up to 0.16 and reached a maximum value 0.070% for BT-*x*(CT-BS) ceramics at *x*=0.16. As further increasing *x* to 0.20, the unipolar strain decreases to 0.034%. The converse piezoelectric coefficient d_{33}^* versus *x* in the inset in Fig. 10 shows the same tendency for strain and reaches the maximum value 1444 pm/V as increasing *x* to 0.16, along with a decreased d_{33}^* as further increasing *x*. The lager strain and d_{33}^* are due to multiphase coexistence of *R*-*O*-*T* at *x*=0.16, which provides for multiple polarization and strain

variants, making it much easier for different grains to coordinate a collective response [27]. A larger strain of 0.070% and corresponding d_{33}^* of 1444 pm/V achieved for BT-x(CT-BS) ceramics is the highest value reported so far in lead-free ceramics, which greatly exceed that of $Ba(Zr_{0.2}Ti_{0.8})TO_3$-$50(Ba_{0.7}Ca_{0.3})TiO_3$ (with strain of 0.057%, d_{33}^* of 1140 pm/V) [8] and all PZT ceramics (with d_{33}^*=360-900 pm/V). This results suggest that BT-x(CT-BS) ceramics is a promising lead-free alternative material for electromechanical actuator applications. Fig. 11 shows the unipolar electric-field-induced strain curves measured at 500 V/mm for BT-x(CT-BS) ceramics at x=0.16 with different temperatures. The strain and d_{33}^* acquire the maximum value 0.070% and 1444 pm/V at 30 ^{o}C, and then decrease as increasing the measured temperature. The decrease of strain and d_{33}^* are due to that the phase structure diverges the region of *R*-*O*-*T* multiphase coexistence as increasing temperature.

Figure 12 shows the relative density and the measured density (a), the piezoelectric coefficient d_{33}, planar electromechanical coupling coefficient k_p and mechanical quality factor Q_m (b) as a function of x for BT-x(CT-BS) ceramics. All the samples show high relative densities over 98%. However, as increasing x, the relative density of samples shows a decreasing trend from 99% at x=0.00 to 98% at x=0.20 in Fig. 12a. Different with the linearly decreased density and grain size as increasing x, d_{33} and k_p have a similar variation tendency shown in Fig. 12b, which first increases and then decreases. Thus, we think, here, that the main effect for the d_{33} and k_p is due to the phase structure. As increasing x, d_{33} and k_p from 280 pC/N and 0.42 at x=0.00 rapidly increase to 570 pC/N and 0.52 at x=0.16, and then decrease to 282 pC/N and 0.22 as further increasing x to 0.20. The giant piezoelectric response d_{33}=570 pC/N at x=0.16 ascribes to *R*-*O*-*T* three-phase coexistence shown in Figs. 4 and 5, which has hardly any energy barrier for polarization rotation and extension between different ferroelectric phases, greatly facilitating the polarization rotation and extension as proposed by Damjanovic[10]. Although the crystalline structure of sample at x=0.20 possesses multiphase coexistence of *R*, *O*/*T* and *C* symmetry which also exhibits a lower energy barrier for polarization rotation, the inferior piezoelectric coefficient d_{33}=282 pC/N was detected. This may be due to

the appearance of paraelectric phase, making ferroelectric domain decreased as shown in Fig.8. The piezoelectric properties of recently reported $BaTiO_3$-based piezoelectric materials are compared in Table I. The extraordinarily large value d_{33}=570 pC/N was achieved in BT-x(CT-BS) ceramics at x=0.16, which is greatly higher than $Ba(Ti_{0.88}Sn_{0.12})O_3-30(Ba_{0.7}Ca_{0.3})TiO_3$ (d_{33}=530 pC/N) [6], $(Ba_{0.98}Ca_{0.02})(Ti_{0.0.96}Sn_{0.04})O_3$ (d_{33}=510 pC/N) [12] and $(Ba_{0.97}Ca_{0.03})(Ti_{0.94}Sn_{0.06})O_3$ (d_{33}=440 pC/N) [13] systems and comparable to PZT-5H, suggesting that BT-x(CT-BS) ceramics are a promising candidate for lead-free piezoelectric ceramics. Compared with the varied d_{33} and k_p with increasing x, Q_m lies in 72-120 as shown in Fig.12b.

Conclusions

A series of BT-x(CT-BS) ceramics (x=0.00, 0.04, 0.08, 0.12, 0.16 and 0.20) lead-free piezoelectric ceramics were prepared by conventional synthesis at 1480 °C. The phase structures were investigated by the XRD, temperature dependence of dielectric constant ε_r and Raman spectra, which changed from *O-T* two-phase coexistence at $0.00 \leq x \leq 0.12$ to *R-O-T* at x=0.16 and then to *R-O/T-C* at x=0.20 multiphase coexistence. The lower E_C=1.31 kV/cm, higher P_r=9.48 μm/cm^2 and larger d_{33}^*=1444 pm/V as well as d_{33}=570 pC/N were achieved at x=0.16, because of *R-O-T* multiphase coexistence. Our results indicate that BT-x(CT-BS) system is a promising candidate for lead-free piezoelectric ceramics.

Acknowledgments

This work was supported by National Natural Science Foundation of China (Grant No. 51332002 and 51221291) and Specialized Research Fund for the Doctoral Program of Higher Education (Grant No. 20130006110006).

References

1. B. Jaffe, W. R. Cook and H. Jaffe, *Academic Press*, New York, 1971.

2. J. Rödel, W. Jo, K. Seifert, E. M. Anton, T. Granzow and D. Damjanovic, *J. Am. Ceram. Soc.*, 2009, **92** (6), 1153–1177.

3. P. K. Panda, *J. Mater. Sci.*, 2009, **44**, 5049–5062.

4. Y. Saito, H. Takao, T. Tani, T. Nonoyama, K. Takatori, T. Homma, T. Nagaya and M. Nakamura, *Nature*, 2004, **432**(7013), 84–87.

5. S. J. Zhang, R. Xia and T. R. Shrout, *J. Appl. Phys*., 2006, **100**,104108.

6. D. Z. Xue, Y. M. Zhou, H. X. Bao, J. H. Gao, C. Zhou and X. B. Ren, *Appl. Phys. Lett.*, 2011, **99**, 122901.

7. C. Zhou, W. F. Liu, D. Z. Xue, X. B. Ren, H. X. Bao, J. H. Gao and L. X. Zhan, *Appl. Phys. Lett.*, 2012, **100**, 222910.

8. W. F. Liu and X. B. Ren, *Phys. Rev. Lett.*, 2009, **103**, 257602.

9. Y. G. Yao, C. Zhou, D. C. Lv, D. Wang, H. J. Wu, Y. D. Yang and X. B. Ren, *EPL*, 2012, **98**, 27008.

10. D. Damjanovic, *Appl. Phys. Lett*., 2010, **97**, 062906.

11. X. S. Wang, H. Yamada, C. N. Xu, *Appl. Phys. Lett.*, 2005, **86**, 022905.

12. W. Li, Z. J. Xu, R. Q. Chu, P. Fu and G. Z. Zang, *J. Am. Ceram. Soc.*, 2011, **94**, 4131–4133.

13. W. Li, Z. J. Xu, R. Q. Chu, P. Fu and G. Z. Zang, *J. Eur. Ceram. Soc.*, 2012, **32**, 517–520.

14. L. F. Zhu, B. P. Zhang, X. K. Zhao, L. Zhao, P. F. Zhou and J. F. Li, *J. Am. Ceram. Soc*., 2013, **96**, 241–245.

15. C. Lei, A. A. Bokov, Z. G. Ye. *J. Appl. Phys.*, 2007, **101**,084105.

16. D. A. Tenne, A. M. Clark, A. R. James, K. Chen and X. X. Xi, *Appl. Phys. Lett.*, 2001,**79**,3836–3838.

17. I. A. Souza, M. F. C. Gurgel, L. P. S. Santos, M. S. Góes, S. Cava, M. Cilense, I. L. V. Rosa, C. O. Paiva-Santos and E. Longo, *Chem. Phys.*, 2006, **322**, 343–348.

18. P. S. Dobal, A. Dixit, R. S. Katiyar, D. Garcia, R. Guo and A. S. Bhalla, *J. Raman Spectrosc*., 2001, **32**, 147–149.

19. I. A. Souza, A. Z. Simões, E. Longo and J. A. Varela, *Mater. Lett*., 2007, **61**, 4086–4089.

20. C. H. Perry and D. B. Hall, *Phys. Rev. Lett.*, 1965, **15**(17), 700–702.

21. B. Piercy, *Trans. Faraday Soc.,* 1959, **55**, 39–51

22. Z. Y. Shen and J. F. Li, *J. Ceram. Soc. Jpn*., 2010, **118**(10), 940-943.

23. K. Bhattacharya and G. Ravichandran, *Acta Mater.*, 2003, **51**(41), 5941–5960.

24. S. T. Zhang, A. B. Kounga, W. Jo, C. Jamin, K. Seifert, T. Granzow, J. Roedel and D. Damjanovic. Adv. Mater., 2009, **21**(46), 4716–4720.

25. R. Z. Zuo, J. Fu, G. Z. Yin, X. L. Li and J. Z. Jiang, *Appl. Phys. Lett.*, 2012, **101**, 092906.

26. J. Fu and R. Z. Zuo, *Acta Mater.*, 2013, **61**,3687–3694.

27. L. F. Zhu, B. P. Zhang, X. K. Zhao, L. Zhao, F. Z. Yao, X. Han, P. F. Zhou and J. F. Li, *Appl. Phys. Lett.*, 2013, **103**, 072905.

Figure Captions

Fig. 1 Phase diagram of BT-CT-BS ternary system near BT-rich corner.

Fig. 2 X-ray diffraction patterns between 2θ range of 20^{o}-70^{o} (a) enlarged ranges of 44^{o}-46^{o} and 65^{o}-67^{o} (b) for BT-x(CT-BS) ceramics.

Fig. 3 Temperature dependence of ε_r for BT-x(CT-BS) ceramics measured at 1 kHz between -50 ^{o}C and 140 ^{o}C.

Fig. 4 Phase diagram of BT-x(CT-BS) ceramics.

Fig. 5 Temperature dependence of the Raman spectra of BT-x(CT-BS) ceramics for x=0.00 (a), and the position of the observed modes (b). The vertical dot line indicates the ferroelectric transition temperature.

Fig. 6 Temperature dependence of the Raman spectra of BT-x(CT-BS) ceramics for x=0.12 (a1, a2), 0.16 (b1, b2) and 0.20 (c1, c2).

Fig.7 SEM images of thermally etched surface for BT-x(CT-BS) ceramics (a) x=0.00; (b) x=0.04; (c) x=0.08;(d) x=0.12 (e) x=0.16; (f) x=0.20

Fig. 8 Ferroelectric hysteresis loops of BT-x(CT-BS) ceramics with $0.00 \leq x \leq 0.20$.

Fig. 9 Strain-electric field (S-E) loops for BT-x(CT-BS) ceramics.

Fig. 10 Electric-field-induced strain and converse piezoelectric coefficient dS/dE for BT-x(CT-BS) ceramics with x=0.00, 0.04, 0.08, 0.12, 0.16, 0.20.

Fig. 11 Electric-field-induced strain and converse piezoelectric coefficient dS/dE for BT-x(CT-BS) ceramics of x=0.16 at different temperatures.

Fig. 12 The relative density and measured density (a), piezoelectric coefficient d_{33}, planar mode eletromechanical coupling coefficient k_p and the mechanical quality factor Q_m (b) as a function of x for BT-x(CT-BS) ceramics.

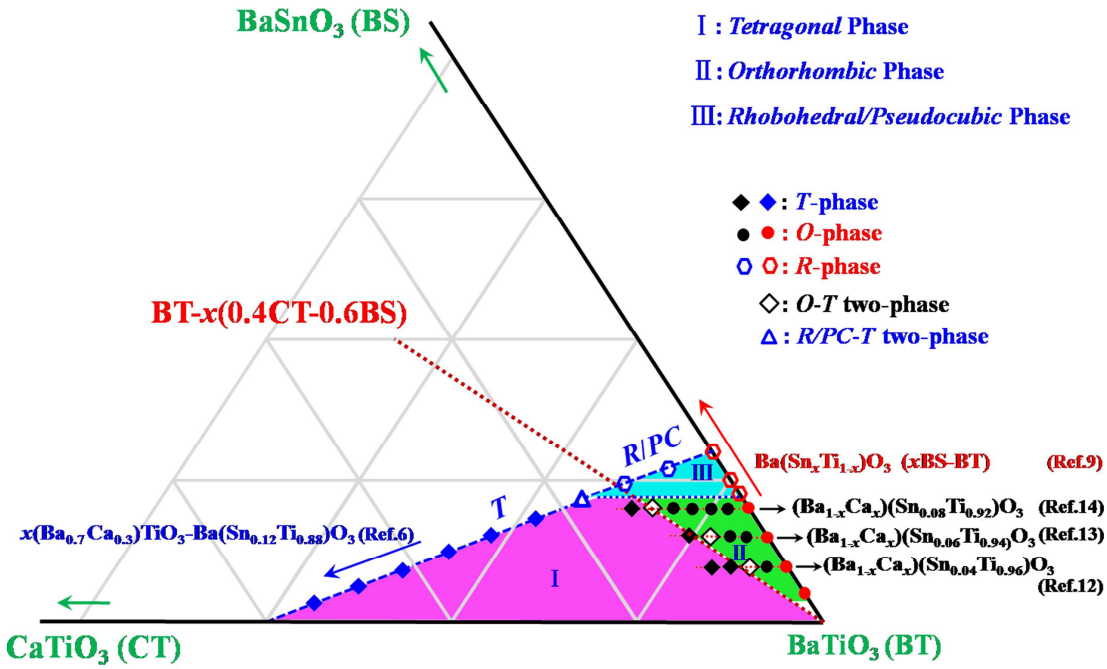

Fig. 1 Phase diagram of BT-CT-BS ternary system near the BT-rich corner.

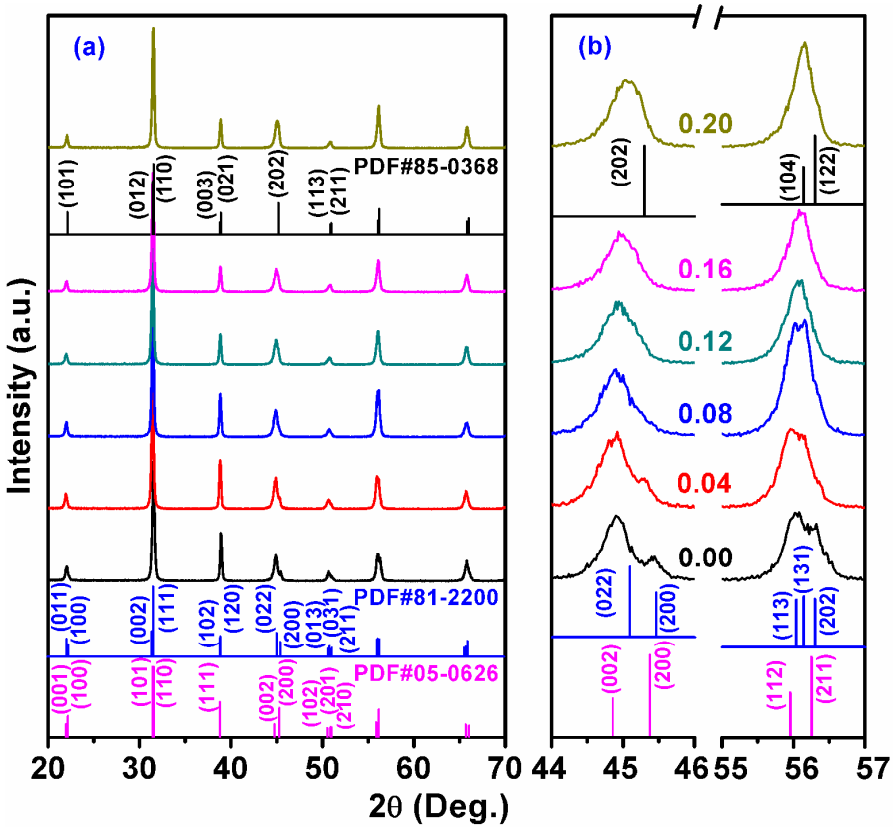

Fig. 2 X-ray diffraction patterns between the 2θ range of 20°-70° (a) enlarged ranges of 44°-46° and 55 °-57 °

(b) for BT-*x*(CT-BS) ceramics..

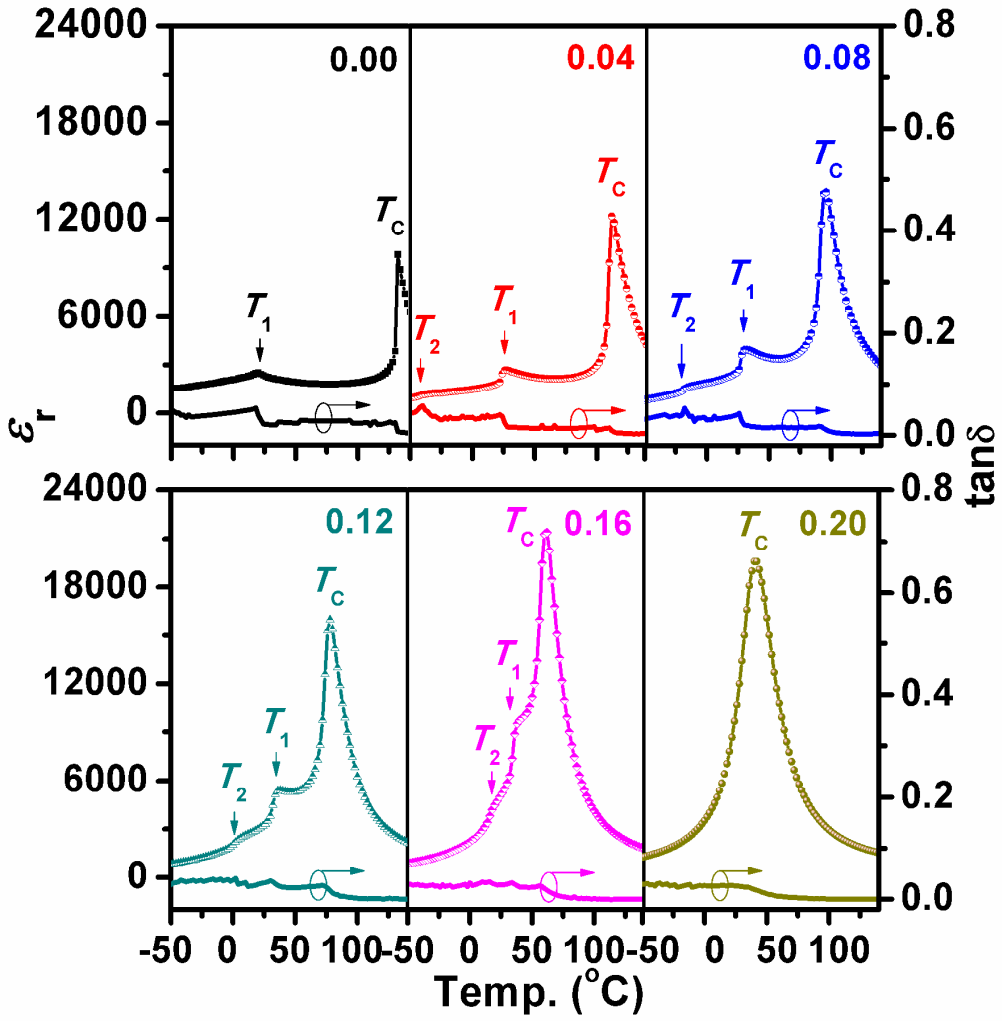

Fig. 3 Temperature dependence of ε_r for BT-x(CT-BS) ceramics measured at 1 kHz between -50 °C and 140 °C.

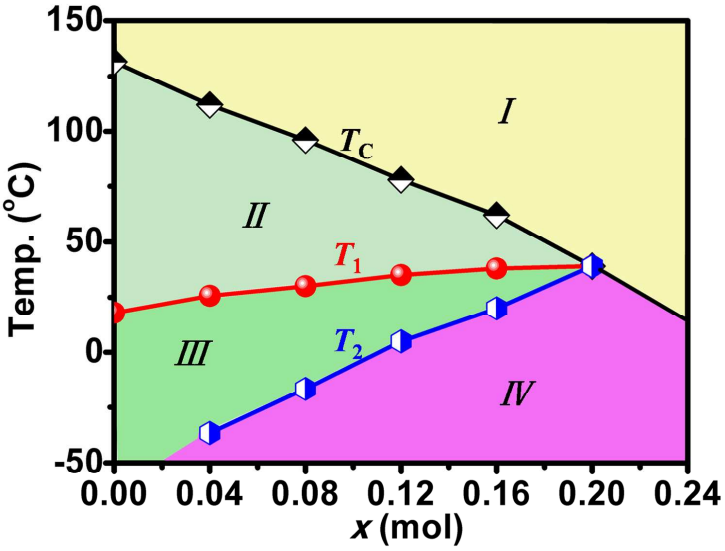

Fig. 4 Phase diagram of BT-x(CT-BS) ceramics.

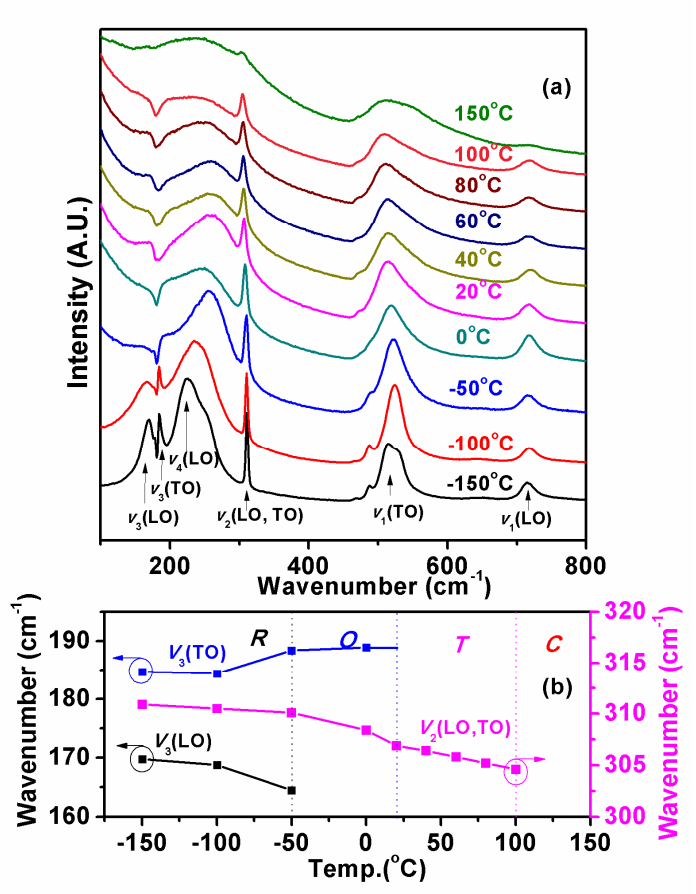

Fig. 5 Temperature dependence of the Raman spectra of BT-x(CT-BS) ceramics for x=0.00 (a), and the position of the observed modes (b). The vertical dot line indicates the ferroelectric transition temperature.

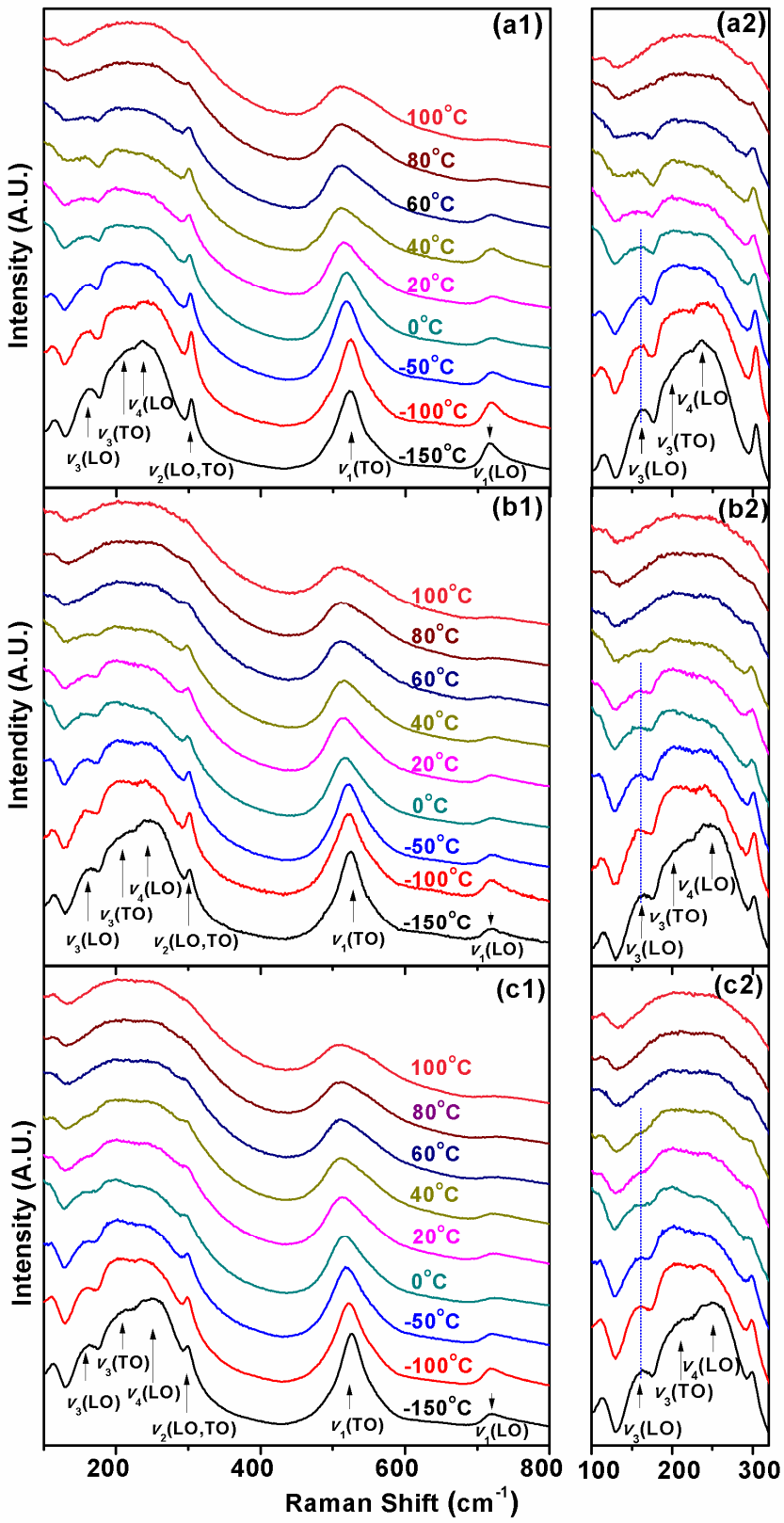

Fig. 6 Temperature dependence of the Raman spectra of BT-x(CT-BS) ceramics for x=0.12 (a1, a2), 0.16 (b1, b2) and 0.20 (c1, c2).

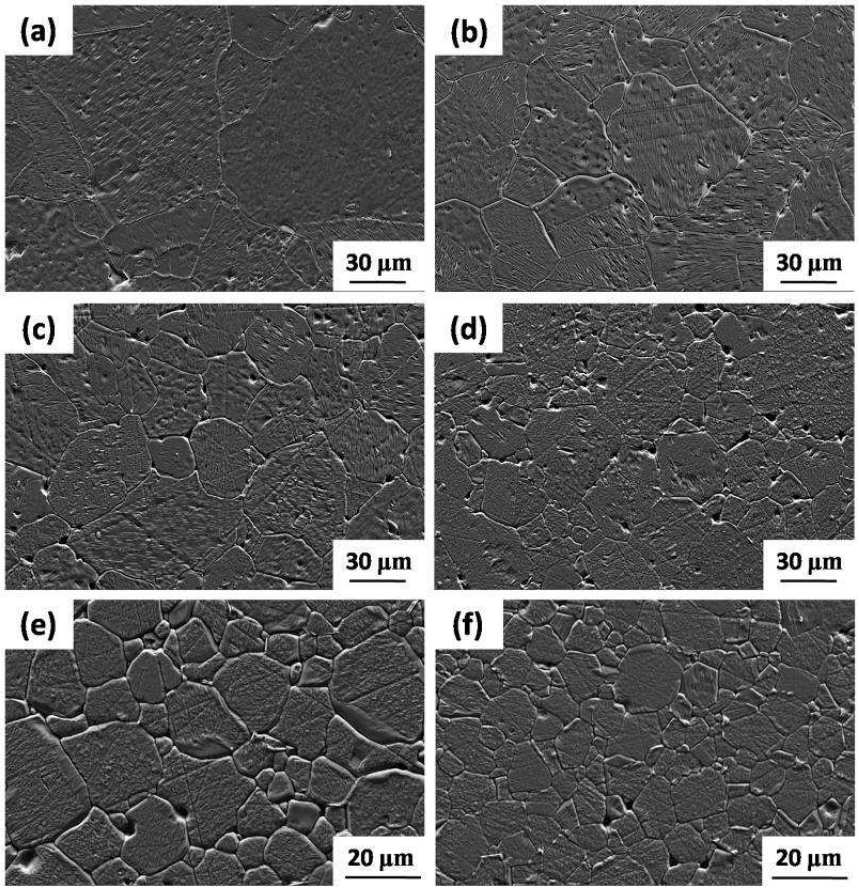

Fig.7 SEM images of thermally etched surface for BT-*x*(CT-BS) ceramics (a) *x*=0.00; (b) *x*=0.04; (c) *x*=0.08;(d) *x*=0.12 (e) *x*=0.16; (f) *x*=0.20

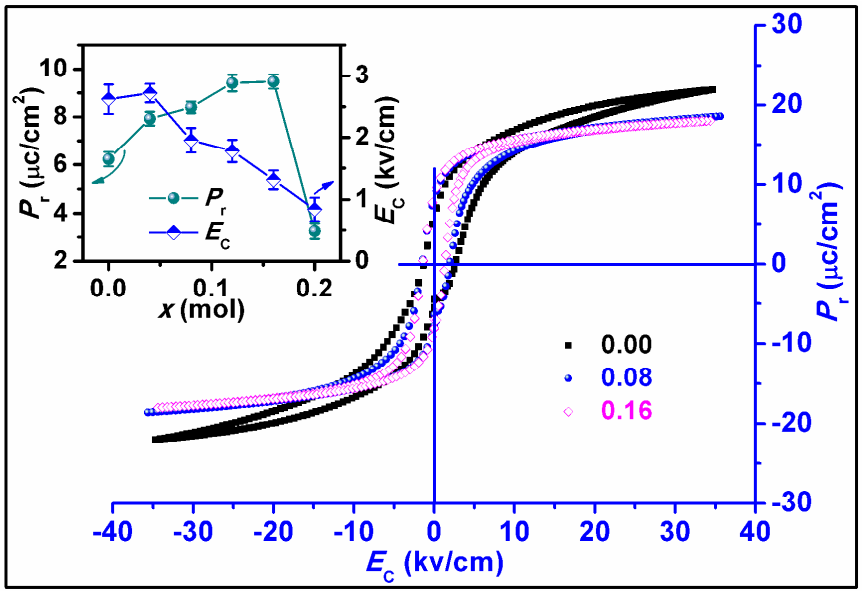

Fig. 8 Ferroelectric hysteresis loops of BT-*x*(CT-BS) ceramics with *x*= 0.00, *x*=0.08 and *x*=0.16.

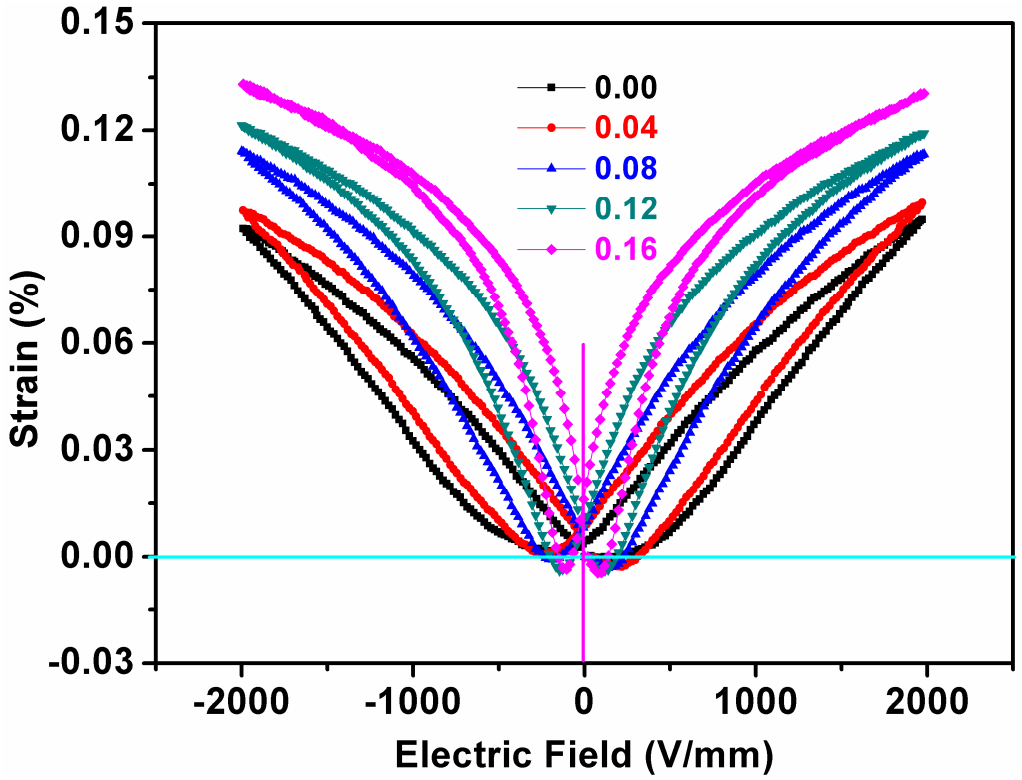

Fig. 9 Bipolar strain curves for BT-*x*(CT-BS) ceramics with *x*=0.00, 0.04, 0.08, 0.12 and 0.16.

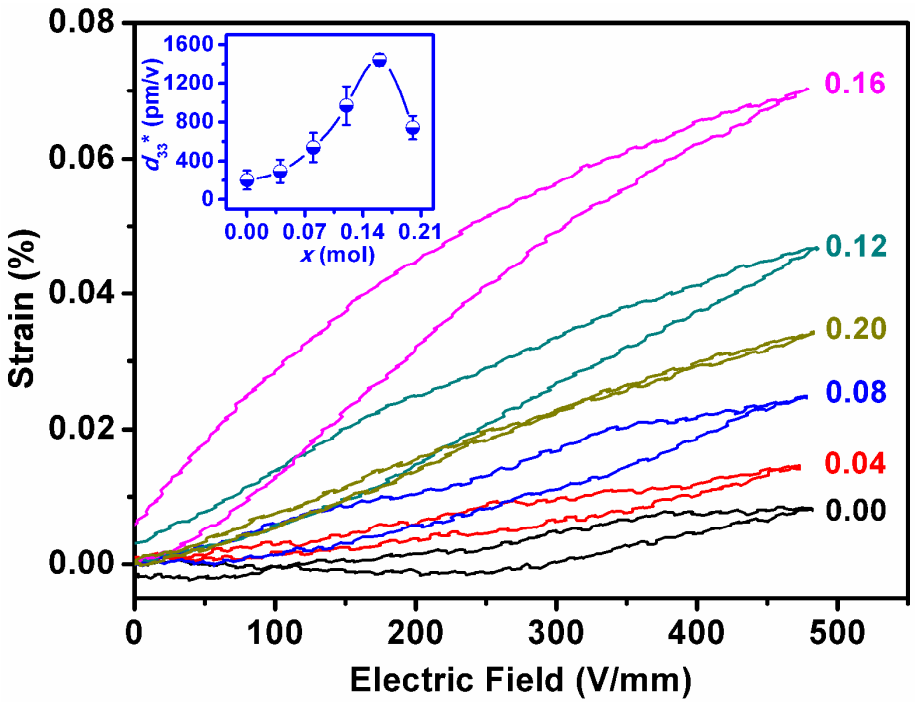

Fig. 10 Unipolar strain curves for BT-*x*(CT-BS) ceramics with *x*=0.00, 0.04, 0.08, 0.12, 0.16 and 0.20.

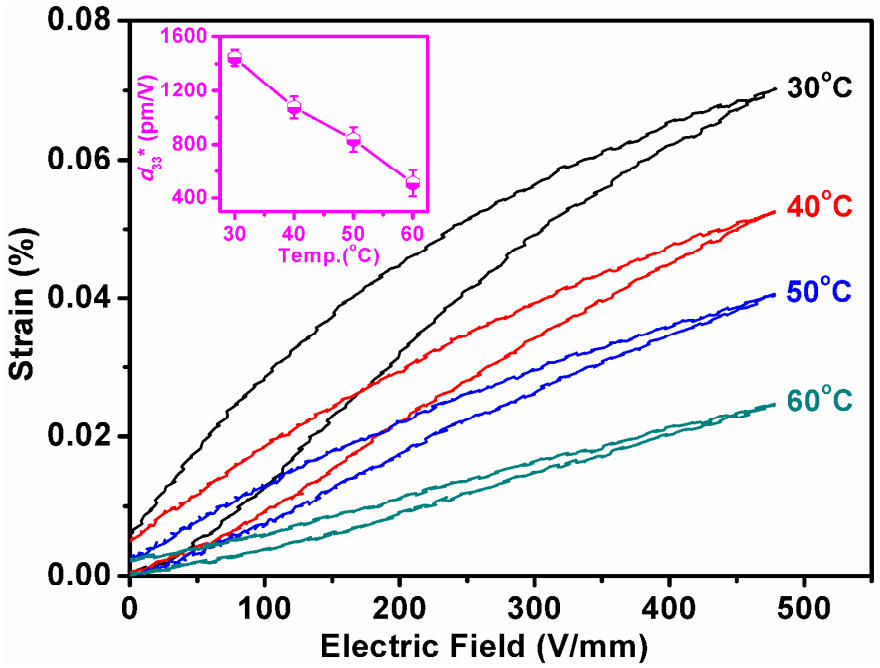

Fig. 11 Unipolar strain curves for BT-x(CT-BS) ceramics at x=0.16 with different temperatures.

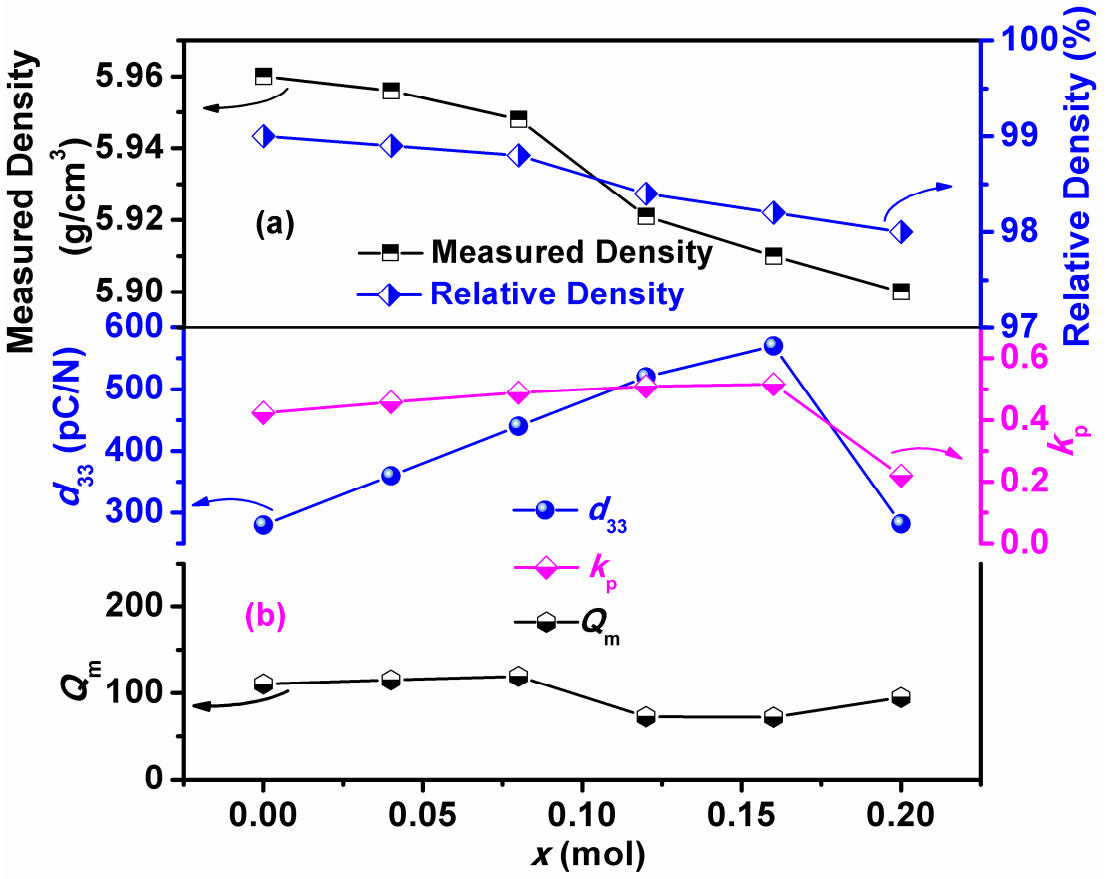

Fig. 12 The relative density and measured density (a), piezoelectric coefficient d_{33}, planar mode eletromechanical coupling coefficient k_p and the mechanical quality factor Q_m (b) as a function of x for BT-x(CT-BS) ceramics.

Table I. The Electrical Properties of recently reported $BaTiO_3$-base Piezoelectric Ceramics

System	d_{33} (pC/N)	k_p (%)	Strain (%)	dE/dS (pm/V)	E_C (kv/cm)	P_r (μC/cm^2)	Ref.
$Ba(Ti_{0.88}Sn_{0.12})O_3-30(Ba_{0.7}Ca_{0.3})TiO_3$	530	55	-	820	3.0	10.7	6
$Ba(Zr_{0.2}Ti_{0.8})TO_3$-50$(Ba_{0.7}Ca_{0.3})TiO_3$	620	-	0.057	1140	1.68	14.5	8
$(Ba_{0.98}Ca_{0.02})(Ti_{0.96}Sn_{0.04})O_3$	510	48	-	-	-	13.2	12
$(Ba_{0.97}Ca_{0.03})(Ti_{0.94}Sn_{0.06})O_3$	440	45	-	-	-	12.2	13
BT-*x*(CT-BS)	570	52	0.070	1444	1.31	9.48	This work

Graphical Abstract

High Piezoelectricity of $BaTiO_3$-$CaTiO_3$-$BaSnO_3$ Lead-Free Ceramics

Li-Feng Zhu, Bo-Ping Zhang, Lei Zhao, Jing-Feng Li

The phase diagram of $BaTiO_3$-$CaTiO_3$-$BaSnO_3$ ternary system near BT-rich corner summarized by a series of recently reported was shown in this figure. A similar phase transformation from *O* to *T* at room temperature was detected in $(Ba_{1-x}Ca_x)(Ti_{0.96}Sn_{0.04})O_3$ ($0.01 \le x \le 0.04$), $(Ba_{1-x}Ca_x)(Ti_{0.94}Sn_{0.06})O_3$ ($0.01 \le x \le 0.04$) and $(Ba_{1-x}Ca_x)(Ti_{0.92}Sn_{0.08})O_3$ ($0.00 \le x \le 0.06$) ceramics. The component of *O* and *T* two-phase coexistence is at x=0.02, 0.03 and 0.05 for above three systems as shown in this figure by symbol "◊", which follows certain component of $(1-x)BaTiO_3$-$x(0.4CaTiO_3$-$0.6BaSnO_3)$ as shown by a dotted line. Compositional zones Ⅰ and Ⅱ indicate *O* and *T* two-phase separated by this $(1-x)BaTiO_3$-$x(0.4CaTiO_3$-$0.6BaSnO_3)$ components. On the other hand, $Ba(Sn_xTi_{1-x})O_3$ and $Ba(Sn_{0.12}Ti_{0.88})O_3$-$x(Ba_{0.7}Ca_{0.3})O_3$ ceramics show a phase transition of *R*-*O* and *R*/*PC*-*T* at x=0.09 and 0.3, respectively, which suggests that *R*-phase is situated in zone Ⅲ. Consequently, it is possible to obtain *R*/*PC*-*O*-*T* multiphase coexistence compositions at room temperature in BT-x(CT-BS) system, which possess high piezoelectric property.